Linking Southern Ocean mixed-layer dynamics to net community production on various timescales

Zuchuan Li[1, 2*], M. Susan Lozier[3], and Nicolas Cassar[1*]

[1] Division of Earth and Ocean Sciences, Nicholas School of the Environment, Duke University, Durham, North Carolina, USA

[2] Applied Ocean Physics and Engineering, Woods Hole Oceanographic Institution, Woods Hole, Massachusetts, USA

[3] School of Earth and Atmospheric Sciences, Georgia Institute of Technology, Atlanta, Georgia, USA

[*] Correspondence to: Zuchuan Li (zuchuanli@gmail.com) and Nicolas Cassar (Nicolas.Cassar@duke.edu)

Key points:

- NCP is correlated with MLD and mixed-layer-averaged PAR on seasonal timescales, and on interannual timescales for spring and winter.
- On intra-seasonal timescales, the impact of mixed-layer dynamics on NCP is most pronounced in the austral spring.
- On longer timescales, NCP is changing in various regions (e.g., around S. America), but no trend is evident for the entire Southern Ocean.

Abstract

Mixed-layer dynamics exert a first order control on nutrient and light availability for phytoplankton. In this study, we examine the influence of mixed-layer dynamics on net community production (NCP) in the Southern Ocean on intra-seasonal, seasonal, interannual, and decadal timescales, using biogeochemical Argo floats and satellite-derived NCP estimates during the period from 1997 to 2020. On intra-seasonal timescales, the shoaling of the mixed layer is more likely to enhance NCP in austral spring and winter, suggesting an alleviation of light limitation. As expected, NCP generally increases with light availability on seasonal timescales. On interannual timescales, NCP is correlated with mixed layer depth (MLD) and mixed-layer-averaged photosynthetically active radiation (PAR) in austral spring and winter, especially in regions with deeper mixed layers. Though recent studies have argued that winter MLD controls the subsequent growing season's iron and light availability, the limited number of Argo float observations contemporaneous with our satellite observations do not show a significant correlation between NCP and the previous-winter's MLD on interannual timescales. Over the 1997-2020 period, we observe regional trends in NCP (e.g., increasing around S. America), but no trend for the entire Southern Ocean. Overall, our results show that the dependence of NCP on MLD is a complex function of timescales.

Plain Language Summary

We examine the influence of mixed-layer dynamics on net community production (NCP) in the Southern Ocean on intra-seasonal, seasonal, interannual, and decadal timescales, using automated observations and satellite data during the period from 1997 to 2020. On intra-seasonal timescales, the shoaling of the mixed layer is more likely to enhance NCP in austral spring and winter. As expected, NCP generally increases with light availability on seasonal timescales. On

interannual timescales, NCP is correlated with mixed layer depth (MLD) and light within the mixed layer in austral spring and winter, especially in regions with deeper mixed layers. Our results do not show a significant correlation between NCP and the previous-winter's MLD on interannual timescales. Over the 1997-2020 period, we observe regional trends in NCP, but no trend for the entire Southern Ocean. Overall, our results show that the dependence of NCP on MLD is a complex function of timescales.

Key words: Net community production, mixed layer depth, Southern Ocean

1. Introduction

Photosynthesis at the ocean surface converts dissolved inorganic carbon into organic matter, part of which is exported to depth [*Volk and Hoffert*, 1985]. The strength of this soft-tissue biological carbon pump is in large part regulated by light and nutrient availability, which to first order are controlled by mixing at the ocean surface.

While a positive correlation between productivity and mixed layer depth (MLD) is generally expected in light-replete, nutrient-limited extrapolar regions [*Wilson and Coles*, 2005], phytoplankton growth in high latitudes may be limited or delayed when mixed layers are sufficiently deep to curtail light availability. On the other hand, the deepening of the mixed layer may be the primary means for the delivery of iron to surface waters in some areas of the Southern Ocean, especially downstream of islands and other hotspot regions [*Bowie et al*., 2015; *McGillicuddy et al*., 2015; *Tagliabue et al*., 2014]. Such opposing effects may explain that both negative and positive correlations between productivity and MLD have been reported in various sectors of the Southern Ocean on intra-seasonal, seasonal, and interannual timescales [*Carranza and Gille*, 2015; *Fauchereau et al*., 2011; *Thomalla et al*., 2011; *Wilson and Coles*, 2005]. Indeed, the tradeoff between light availability and the entrainment of subsurface iron [*Carranza and Gille*, 2015; *Cassar et al*., 2011; *Mitchell and Holm-Hansen*, 1991; *Mitchell et al*., 1991; *Nelson and Smith*, 1991; *Tagliabue et al*., 2014] may explain the spatiotemporal variability of productivity in response to MLD changes, thereby producing a time-scale dependent relationship between productivity and MLD in the Southern Ocean.

To explore the relationship between MLD and productivity in the Southern Ocean, we use satellite data to reconstruct net community production (NCP) variability from 1997 to 2020. NCP is defined as the difference between net primary production (NPP) and heterotrophic respiration

and represents the organic carbon available for export [*Li and Cassar* 2017]. Based on this reconstruction, we examine the relationship (and trends) of satellite-derived NCP estimates to MLD, and to mixed-layer-averaged photosynthetically active radiation (PAR) on seasonal and interannual timescales. We also use biogeochemical Argo floats to examine the impact of mixed-layer dynamics on productivity on intra-seasonal timescales. This study is particularly timely considering the pivotal role played by the Southern Ocean in the oceanic carbon sink [*Fletcher et al*., 2006; *Frolicher et al*., 2015; *Sabine et al*., 2004] and in light of recent studies suggesting that a strengthening of the Southern Ocean carbon sink over the last decade is potentially due to weakened ventilation or increased stratification [*Landschutzer et al*., 2015; *Majkut et al*., 2014; *Munro et al*., 2015]. These physical changes may influence nutrient and light availability, which in turn impact productivity and hence the carbon sink in the Southern Ocean. Moreover, because of the decreasing buffering capacity of seawater as CO_2 rises, the contribution of the biological pump to the carbon sink in the Southern Ocean is expected to increase in the future, even without any change in primary production [*Hauck and Volker*, 2015]. In this context, an improved understanding of the factors regulating NCP on different timescales is warranted.

2. Methods and data

2.1. Data

2.1.1. *In situ* observations

MLD was estimated from the temperature and salinity profiles of Argo in the Southern Ocean (≥ 35°S) from 2001 to 2020. Temperature-salinity profiles, downloaded from http://www.usgodae.org/, were retained only if marked with a quality flag of '1' ('good data') or '2' ('probably good data'). This filtering process led to 427,000 profiles evenly partitioned among austral spring (24%), summer (26%), autumn (26%), and winter (24%). Using the filtered

profiles, we calculated MLD as the depth at which the potential density (σ_θ) exceeds a near-surface (10 m) reference value by $\Delta\sigma_\theta = 0.03$ kg m^{-3} [*de Boyer Montegut et al*., 2004; *Dong et al*., 2008]. The MLD estimates were averaged to obtain daily 2° grids, which were used to calculate monthly-averaged fields and monthly climatologies and anomalies.

We explored the impact of transient mixed-layer changes on the variation in chlorophyll *a* concentration ([Chl]) and particulate organic carbon (POC) using biogeochemical Argo floats from the Southern Ocean Carbon and Climate Observations and Modeling (SOCCOM) project. We downloaded 163 SOCCOM biogeochemical Argo floats with observations between March 2014 and December 2020 from https://soccom.princeton.edu/. These floats consist of 15240 profiles, among which 8490 profiles have [Chl] with a quality flag of '0' ('good data'). Each profile has temperature, salinity, [Chl], and backscatter measurements. Temperature and salinity were used to derive MLD based on the same criteria as for other Argo floats (see description above). [Chl] was corrected for nonphotochemical quenching [*Boss and Haentjens*, 2016]. Median value of [Chl] below 600 dbar from each profile was subtracted from the profile as in *Uchida et al*. [2019]. Backscatter at 700 nm was used to derive POC [*Boss and Haëntjens*, 2016]. The relationship between backscatter, POC, [Chl] and phytoplankton carbon biomass bears uncertainties [*Boss and Haentjens*, 2016; *Johnson et al*., 2017]. While random errors introduce noise in the observed relationships, potential biases in our proxies from biogeochemical Argo floats should not significantly impact our analysis because we are calculating differences in signal. Seasons are defined as follows: austral spring (September-November), summer (December-February), autumn (March-May), and winter (June-August).

2.1.2. Satellite observations

We estimated [Chl] using algorithms specific to the Southern Ocean [*Johnson et al*., 2013]:

$$[Chl] = 10^{\left(0.6736-2.0714R_{SW}-0.4939R_{SW}^2+0.4756R_{SW}^3\right)} \qquad (1)$$

$$[Chl] = 10^{\left(0.6994-2.0384R_{MA}-0.4656R_{MA}^2+0.4337R_{MA}^3\right)} \qquad (2)$$

where $R_{SW} = log10\big(Rrs(443/555) > Rrs(490/555) > Rrs(510/555)\big)$ and $R_{MA} = log10\big(Rrs(443/555) > Rrs(490/555)\big)$ represent the maximum of the band ratios for the SeaWiFS and MODIS-Aqua, respectively; and $Rrs(r_1/r_2) = \frac{Rrs(r_1)}{Rrs(r_2)}$ represents band ratio at the wavelengths of r_1 and r_2. Daily and monthly level-3 $Rrs(\lambda)$, acquired by SeaWiFS (1997-2010) and MODIS-Aqua (2002-2020), were downloaded from NASA's ocean color website (http://oceancolor.gsfc.nasa.gov/). The *Rrs*(λ) have a spatial resolution of $0.083° \times 0.083°$.

We derived maps of NPP based on satellite [Chl], PAR, sea surface temperature (SST), and the VGPM model of *Behrenfeld and Falkowski* [1997]. VGPM estimates NPP over the euphotic zone as the product of the maximum photosynthetic rate of phytoplankton, light availability (including the length of the photoperiod), and the chlorophyll inventory within the euphotic zone (see equation (10) in *Behrenfeld and Falkowski* [1997]). The maximum photosynthetic rate of phytoplankton is modeled as an empirical function of temperature through a polynomial regression. The chlorophyll inventory indicates the phytoplankton biomass assuming a constant chlorophyll to carbon ratio. The uncertainties associated with the VGPM model are discussed in the supplementary material (see also *Behrenfeld and Falkowski* [1997]). Satellite PAR images with a spatial resolution of $0.083° \times 0.083°$ were downloaded from NASA's ocean color website. Monthly SST acquired by AVHRR (1997-2007) and MODIS-Aqua (2002-2020), were downloaded from NOAA's NODC website (http://www.nodc.noaa.gov/SatelliteData/pathfinder4km/) and NASA's ocean color website, respectively.

Based on NPP and SST, we derived NCP using the algorithm developed by *Li and Cassar* [2016]:

$$\mathrm{NCP} = \frac{8.57 \times NPP}{17.9 + SST} \qquad (3)$$

where NCP and NPP have units of mmol O_2 m^{-2} d^{-1}, and SST is in degree Celsius (^{o}C). Satellite NPP estimates are converted from C to O_2 units using a stoichiometry of O_2/C=1.4 [*Laws*, 1991]. Equation (3) was derived using the machine learning approach of genetic programming (GP) based on a large dataset of O_2/Ar-NCP observations in the Southern Ocean [*Li and Cassar*, 2016]. GP searches for optimal predictors and functional forms of NCP based on a set of environmental variables and O_2/Ar-NCP observations. Equation (3) has an acceptable validation accuracy (mean squared error of 190.46 and coefficient of determination of 0.68). In terms of overall model performance evaluated using O_2/Ar-NCP observations, equation (3) is comparable to or outperforms prior algorithms for the world's ocean [*Li and Cassar*, 2016]. However, NCP estimates may be biased in the austral winter and in regions where upwelling and mixing are strong. A more thorough discussion of uncertainties associated with equation (3) is presented in the supplementary material. Our satellite-NCP estimates can be accessed online at https://sites.nicholas.duke.edu/cassar/remote-sensing-export.

For comparison, we also derived carbon export production at the euphotic depth and 100m depth using the global algorithms developed by *Laws et al*. [2000] and *Dunne et al*. [2005], a NCP algorithm specific to the Southern Ocean [*Chang et al*., 2014], and a regional NCP algorithm specific to the Western Antarctic Peninsula in the Southern Ocean [*Li et al*., 2016]. The estimates from these algorithms show similar patterns (see Figure S1), but there are differences in part due to models being trained with different datasets. A comparison of export production estimates in the Southern Ocean can be found in *Arteaga et al*. [2018]. A discussion

on the influence of depth of integration on export production can be found in *Li and Cassar* [2018].

Climatological mixed-layer-averaged PAR (PAR_{ml}) was derived using surface PAR, $[Chl]$ and the diffusion attenuation coefficient estimated using the algorithm developed by *Morel et al*. [2007]. The equation for PAR_{ml} can be found in *Bender et al*. [2016].

2.2. Methods

2.2.1. Intra-seasonal variability

We calculate MLD and POC differences between sequential profiles from the same biogeochemical Argo float with a ~10 day interval. For pairs with a shoaling mixed layer, POC change is calculated as $\Delta POC = log\left(\frac{\sum_{i=0}^{MLD_{t+1}} POC_{t+1}^{i}}{MLD_{t+1}}\right) - log\left(\frac{\sum_{i=0}^{MLD_{t}} POC_{t}^{i}}{MLD_{t}}\right)$, where MLD_t (MLD_{t+1}) represents MLD at time t ($t+1$), and POC_t^i (POC_{t+1}^i) at depth i represents POC at time t ($t+1$). Terms $log\left(\frac{\sum_{i=0}^{MLD_{t+1}} POC_{t+1}^{i}}{MLD_{t+1}}\right)$ and $log\left(\frac{\sum_{i=0}^{MLD_{t}} POC_{t}^{i}}{MLD_{t}}\right)$ represent logarithmic averages of POC over mixed layer at time $t+1$ and t, respectively. We note that the impact of horizontal advection on ΔPOC is not considered.

The POC change can be related to NCP through the mass balance of organic matter at the ocean surface:

$$\frac{d(MLD \times (POC + DOC))}{dt} = NCP - export \qquad (4)$$

where DOC represents dissolved organic carbon. Over seasonal timescales, because the change in the inventory of organic matter at the ocean surface is small, NCP is a good approximation of export. Over the timescales of ~week, the change in POC reflects the balance between NCP and

export. Our analyses of the ΔPOC should therefore be interpreted with caution as no change in POC could reflect no response to changes in MLD, or balanced NCP and export.

2.2.2. Seasonal and interannual variability

Monthly climatological NCP is calculated as the mean NCP for each month from 1997 to 2020, with missing values excluded. NCP interannual variability is estimated by subtracting the monthly climatological NCP from the monthly NCP time series from the same time period. We refer to these values as the NCP anomalies. To examine controls on NCP on seasonal and interannual timescales, we calculate the Spearman correlation between NCP anomalies and physical parameters that include MLD and mixed layer averaged PAR. The Spearman correlation between two variables is the Pearson correlation between the rank values of these variables. Thus, the Spearman correlation between NCP anomalies and physical parameters measures their monotonical relationship (whether linear or not).

2.2.3. Trends

To assess the trends in NCP integrated over the entire growing season, we derive annual NCP estimates in individual grids by summing monthly NCP for each year. Missing values in monthly NCP are linearly interpolated with values in adjacent months and are set to NaN when NCP in adjacent months is also missing value. Satellite-derived time series of annual NCP (1997-2020) have 23 discrete year values. To derive relationships with statistical meaning, we increase the number of samples per grid by grouping geographically adjacent annual NCP into 5° in latitude by 10° in longitude grids. Within each grid, the time series of annual NCP ($ANCP_{i,j,k}$) is modeled as a linear function of year (yr_k) using the Bayesian hierarchical model to share information across sub-grids:

$$ANCP_{g,i,k} \sim Normal(\beta_g^1 * yr_k + \beta_g^0, \sigma^2) \qquad (5)$$

$$\beta_g^0 \sim Normal(\mu_0, \sigma_0^2) \qquad (6)$$

$$\beta_g^1 \sim Normal(\mu_1, \sigma_1^2) \qquad (7)$$

where g, i, and k represent group, sample indices, and year, respectively; and β_g^1 describes the trend of annual NCP. μ_0 and μ_1 have priors of Normal(0, 0.0001). σ^2, σ_0^2, and σ_1^2 have priors of $Unif(0,100)$ where $Unif$ represents a uniform distribution.

We simulate posterior distributions of model parameters using a Markov Chain Monte Carlo (MCMC) method. MCMC is a group of algorithms for sampling from a probability distribution, through which we can create a sequence of samples to approximate the posterior distribution of slope and intercept in equations (5-7). The sequence contains 10000 iterations, with the last 5000 samples (burn-in=5000) for calculating mean and variance of posterior distributions of slope and intercept. A good approximation to a distribution requires the simulation to converge to the stationary distribution. Otherwise, error will be introduced into the estimated trend (i.e., slope) in NCP. The model is implemented using the package of WinBUGS [*Lunn et al*., 2000].

3. Results and discussion

Previous studies have shown that the Southern Ocean's high-nutrient, low-chlorophyll (HNLC) regime stems from the complex interplay of grazing, light, and iron limitation of primary production [*Boyd et al*., 2007; *Frost*, 1991; *Martin et al*., 1990; *Mitchell et al*., 1991; *Nelson and Smith*, 1991]. There are multiple sources of iron in the Southern Ocean: atmospheric deposition [*Boyd and Ellwood*, 2010; *Cassar et al*., 2007; *Duce and Tindale*, 1991], upwelling of iron-rich subsurface water due to the interaction of currents with topography [*Sokolov and Rintoul*, 2007] and entrainment during winter mixing [*Tagliabue et al*., 2014], horizontal advection of iron-rich water from continental shelves [*Graham et al*., 2015; *Robinson et al*., 2016], and sea-ice and glacial melt in high-latitude regions [*Lannuzel et al*., 2007; *Lannuzel et al*.,

2008]. In addition, iron may be supplied to subantarctic waters through horizontal advection of iron-rich subtropical waters. As noted in previous studies, low macronutrient availability in subtropical waters likely limits phytoplankton consumption of iron in these waters [*Bowie et al*., 2009; *Cassar et al*., 2011].

Grazing pressure, and iron and light availability are in turn partly set by mixed-layer dynamics. Below, we derive spatial patterns of climatological NCP and link NCP variability to mixed-layer dynamics on intra-seasonal, seasonal, interannual timescales and long-term trends, but we first start by describing the climatology of NCP in the Southern Ocean.

3.1. Climatology

The geographical variability of our derived climatological mean NCP is generally consistent with other NCP and primary production estimates (e.g., NCP from *Chang et al.* [2014] and NPP derived by *Arrigo et al*. [2008]). High NCP values are observed near the Subtropical Front between 40°S and 50°S, as well as along coasts, across shelf regions, and downstream of islands such as the Kerguelen Islands, New Zealand, and Southern Georgia (Figure 1). Annual NCP is generally higher in the Atlantic sector than in the eastern Pacific. When light is replete, some combination of iron sources likely drives the elevated NCP we observe. In contrast, low NCP regions are generally located far from continents (e.g., eastern Pacific), with low atmospheric deposition and weak sources from below.

Varying seasonality in NCP leads to relatively weak geographical variability in the annual average NCP. For example, regions near the Antarctic coast (e.g., Ross Sea, Western Antarctic Peninsula, and Weddell Sea) display high primary production rates in austral summer, as reported in previous studies [*Arrigo et al*., 2008; *Arrigo et al*., 2015; *Li et al*., 2016]. However, because of the shorter growing season in these regions, rates are more comparable to those in

lower-latitude regions when integrated over the entire year. While the growing season only lasts about 3 months in the Antarctic shelf regions, it may extend beyond 6 months in the northern portions of the Atlantic sector (see Figure S2).

3.2. Intra-seasonal

In this section, we explore how mixed layer dynamics impact POC as a function of season. The POC response to mixed layer dynamics ultimately depends on the relation of the mixed layer to the critical depth, defined as the depth at which the depth-integrated NPP is equal to heterotrophic respiration. When the mixed layer is deeper (shallower) than the critical depth, POC is expected to decrease (increase) in a light-limited system. In our study, we use the surface PAR and the light attenuation coefficient to estimate the critical depth based on equation (6) in *Nelson and Smith* [1991], with the caveat that such estimates carry significant errors, most notably associated with the difficulty in estimating the community respiration and compensation depth (see *Nelson and Smith* [1991] for further description of the uncertainties).

These first-order estimates show that the critical depth varies latitudinally in the Southern Ocean and across seasons (see Figure S3). As expected, deep critical depths generally occur in the summer, and in subtropical waters and the northern portions of the Pacific subantarctic waters. Recent studies have shown that NCP in high latitude oceans is consistently low when mixed layers are deep, presumably because deeper mixed layers extend beyond the critical depth [*Cassar et al*., 2011; *Eveleth et al*., 2016]. Our results agree with these studies, with the POC concentration in the mixed layer displaying an heteroscedastic relationship to MLD, with large variability in POC concentrations in shallower mixed layers, and consistently low POC concentrations in deeper mixed layers (Figure 2). The mechanisms behind the heteroscedasticity of NCP vs. MLD are further explained by the modeling work of *Li and Cassar* [2017].

In dynamic terms, POC is more likely to increase in response to mixed layer shoaling above the critical depth in the spring and winter when iron is less likely to be limited (Figure 3). During the other seasons, the response is somewhat split at around 50%, suggesting that during these other seasons, the mixed layer shoaling may not force POC changes (especially in the summer when 99% of the MLD observations are shallower than the critical depth), or may drive forcings (e.g., light, grazing and iron) in opposite directions, thereby canceling their overall impact on POC changes. [Chl] from biogeochemical Argo floats show similar results (see Figure S4). Overall, our results are in line with *Llort et al*. [2019] in that they reveal a complex response of POC to shoaling mixed layers.

3.3. Seasonal

As expected, NCP is highly correlated to MLD and PAR_{ml} on seasonal timescales (Figure 4). In austral winter, deep winter mixing and high solar zenith angle generally limit NCP, while in austral spring and summer, increasing insolation and shoaling mixed layers increase light availability and NCP [*Li and Cassar*, 2018]. However, the correlations between NCP, MLD, and PAR_{ml} break down at lower-latitudes (north of the subtropical front, generally north of 40°S), where productivity is likely also limited by macronutrient availability. The correlation between NCP and MLD is also lower in some regions of the Pacific sector (50-60°S, 60-150°W) where grazing is believed to regulate phytoplankton productivity as diagnosed from model simulations [*Rohr et al., 2017*].

NCP displays a stronger correlation with PAR_{ml} than MLD. NCP is controlled by light availability in the mixed layer, which is a function of incident PAR and MLD [*Bender et al*., 2016]. Consequently, low NCP is observed in the Pacific sector in the austral autumn when MLDs are still fairly shallow but surface PAR is low (see Figure S5).

3.4. Interannual

NCP monthly anomalies are weakly correlated to MLD and PAR_{ml} anomalies in some regions (Figure 5). Correlation is generally observed in the subantarctic region of the Pacific and Indian sectors in austral spring and winter when the mixed layer is deep (Figures 5, S5 and S6). For example, 97% and 87% of grids with seasonal MLD≥150m show a negative correlation between monthly anomalies of MLD and NCP in austral spring and winter, respectively. Similarly, 89% and 74% of grids with seasonal MLD≥150m show a positive correlation between monthly anomalies of PAR_{ml} and NCP in austral spring and winter, respectively. The negative correlation to MLD is consistent with decreased light availability and increased depth-integrated heterotrophic respiration compared to photosynthesis due to a deeper mixed layer, while the positive correlation to PAR_{ml} is likely attributable to increased light availability.

Our analyses have focused so far on synchronous changes in monthly MLD and NCP, yet prior studies have hypothesized that deep winter mixing supports productivity in the subsequent growing season because of the entrained iron [*Fauchereau et al*., 2011; *Tagliabue et al*., 2014; *Thomalla et al*., 2011]. Because shallow winter mixed layers are not expected to reach the deep ferricline, low iron in the mixed layer would result. Based on our analyses of the limited number of Argo observations (less than 20 in most grids; see Figure S7), we do not find statistically significant correlations between winter MLD and average NCP in both austral spring and summer (Figure 6). Other than uncertainties in our derived proxies, this lack of correlation has four possible explanations, akin to those given above for the weak correlations between synchronous changes in MLD, PAR_{ml} and NCP. First, while mixed layer deepening likely entrains iron from the subsurface, iron may also be supplied through the other pathways mentioned above. For example, iron can be brought to the euphotic layer via mesoscale and

submesoscale isopycnal stirring in the open Southern Ocean [*Uchida et al*., 2019; *Uchida et al*., 2020] and storm-driven vertical mixing [*Carranza and Gille*, 2015]. Second, deepening of the mixed layer may be insufficient to mine iron from the subsurface (ferricline may be as deep as 333m [*Tagliabue et al*., 2014]). As has been shown in previous studies [*Dave and Lozier*, 2013; *Lozier et al*., 2011; *Tagliabue et al*., 2014], the supply of nutrients to the surface depends not just on the depth of the mixing, but on the degree to which nutrients are available at depth [*Llort et al*., 2019]. Third, elevated iron availability through deepening of the mixed layer may be counteracted by decreasing light availability because of decreasing NCP maximum with increasing MLD [*Li and Cassar*, 2017]. Finally, the influence of light availability on NCP may be offset by changes in phytoplankton biomass concentration, which can be seen in the relationship between chlorophyll-normalized NCP and PAR_{ml} in *Bender et al*. [2016] and *Li and Cassar* [2017]. For example, the increase in biomass will lead to an increase in biomass-driven light attenuation, the net effect of which depends on the relative impacts of the changes in light availability and biomass inventory on NCP [*Li and Cassar*, 2018]. We note that our analysis (MLD and PAR_{ml}) does not explicitly consider zooplankton grazing [*Behrenfeld et al*., 2010], which is believed to exert control on productivity during some parts of the year and in some regions of the Southern Ocean [*Le Quéré et al*., 2016]. Therefore, the relation of NCP to PAR_{ml} does not necessarily hold should other factors, such as nutrient availability and grazing, be first-order controls on NCP (unless they correlate with PAR_{ml}).

3.5. Long-term trends

Mean annual NCP is estimated to be 3.91±0.16 Pg C yr^{-1} south of 35°S (Figure 7). As shown in *Li and Cassar* [2016], our algorithms generally predict higher NCP in the Southern Ocean than some of the other models. No statistically significant trend for the annual NCP between

1997 and 2020 is evident for the entire region. However, annual NCP displays varying regional trends, though they account for less than 10% of the interannual variability in each region. Annual NCP between 40°S and 60°S in the Atlantic sector increased ~0.25 g C m^{-2} yr^{-1} over the record, equivalent to an ~6% increase per decade. Increasing trends are also observed southeast of Australia (~4% per decade) and in the regions south of 60°S (~5% per decade). In general, we observe weak decreasing trends in the subantarctic frontal zones outside of the Atlantic sector.

Our estimated trends in annual NCP are spatially consistent with trends in the CO_2 sinks described by *Landschutzer et al*. [2015]. Trends in annual NCP corresponding to the time period used in that study (from 2002 to 2011) can be found in Figure S8. Their reported decrease in the non-thermal CO_2 sink in the Pacific sector between 2002 and 2011 is generally consistent with a reduction in NCP, and the corresponding increase in the CO_2 sink in the Atlantic is consistent with an NCP increase. However, we show here that NCP is not a contributor to the observed trend in CO_2 sink over the entire spatial domain. The overall increasing CO_2 sink estimated by *Landschutzer et al*. [2015] is possibly the result of a change in the ventilation of CO_2-rich deep waters. We do not find a statistically significant trend in annual NCP in the Drake Passage, where an intensification in the CO_2 sink has been hypothesized to originate from decreasing temperatures in austral summer and the absence of change in austral winter dissolved inorganic carbon (DIC) [*Munro et al*., 2015]. Our NCP trends are consistent with NPP trends in the Ross Sea [*Schine et al*., 2016]. *Kahru et al*. [2017] found a consistent trend of increasing NPP from 2002 to 2011 in the Atlantic sector. They attribute changes in NPP, including a decreasing trend in NPP in the same region from 2011 to 2016 to a shift in the phytoplankton community.

4. Conclusions

In this study, we explored intra-seasonal, seasonal, interannual variability and longer-term trends in NCP in the Southern Ocean during the period from 1997 to 2020. Although our analyses carry uncertainties and limitations (see supplement), general patterns are identified. Our findings corroborate earlier studies showing that NCP is generally high in the Atlantic sector and downstream of islands. While NCP is high in austral summer across Antarctic continental shelves, as highlighted in other studies, our work shows that it is comparable to or lower than NCP in some lower-latitude regions when integrated over the entire year because of the short growing season. We find that the impact of mixed-layer dynamics on NCP is a function of timescales. On intra-seasonal timescales, the impact of mixed-layer dynamics on NCP varies across the season, with NCP increasing with mixed layer shoaling in austral spring and winter. As expected on seasonal timescales, NCP variability is likely controlled by light availability. On interannual timescales, NCP is correlated to MLD and mixed-layer-averaged PAR in deep-mixed-layer region in austral spring and winter. Contrary to recent studies, our preliminary results also show no clear association between deep winter mixing and NCP in the subsequent growing season. We did not find statistically significant trends in integrated annual NCP for the entire Southern Ocean, but we did find local trends in annual NCP across the Southern Ocean. Additional observations, especially the ones provided by the biogeochemical Argo floats, will help further unravel the multitude of factors driving these multiscale patterns and trends.

Acknowledgements

We would like to acknowledge NASA GSFC for processing and distributing the SeaWiFS and MODIS-Aqua products (http://oceancolor.gsfc.nasa.gov/). Global Argo data were downloaded from http://www.usgodae.org/. Biogeochemical Argo float data were collected and made freely available by the Southern Ocean Carbon and Climate Observations and Modeling (SOCCOM)

Project funded by the National Science Foundation, Division of Polar Programs (NSF PLR - 1425989 and OPP-1936222), supplemented by NASA, and by the International Argo Program and the NOAA programs that contribute to it. Work was supported by NSF OPP-1043339 to N.C. and NASA NNX13AC94G to M.S.L. Z.L. was supported by a NASA Earth and Space Science Fellowship (Grant No. NNX13AN85H) and the Postdoctoral Scholarship Program at Woods Hole Oceanographic Institution.

References

Arrigo, K. R., G. L. van Dijken, and S. Bushinsky (2008), Primary production in the Southern Ocean, 1997-2006, Journal of Geophysical Research-Oceans, 113(C8).

Arrigo, K. R., G. L. van Dijken, and A. L. Strong (2015), Environmental controls of marine productivity hot spots around Antarctica, Journal of Geophysical Research-Oceans, 120(8), 5545-5565.

Arteaga, L. A., N. Haëntjens, E. Boss, K. S. Johnson, and J. L. Sarmiento (2018), Assessment of export efficiency equations in the Southern Ocean applied to satellite-based Net Primary Production, Journal of Geophysical Research-Oceans, 123(4), 2945-2964.

Behrenfeld, M. J., and P. G. Falkowski (1997), Photosynthetic rates derived from satellite-based chlorophyll concentration, Limnology and Oceanography, 42(1), 1-20.

Behrenfeld, M. J. (2010), Abandoning Sverdrup's critical depth hypothesis on phytoplankton blooms, Ecology, 91(4), 977-989.

Bender, M., B. Tilbrook, N. Cassar, B. F. Jonsson, A. Poisson, and T. Trull (2016), Ocean productivity south of Australia during spring and summer, Deep-Sea Res, 112, 68-78.

Boss, E.B. and N. Haëntjens (2016), Primer regarding measurements of chlorophyll fluorescence and the backscattering coefficient with WETLabs FLBB on profiling floats. SOCCOM Tech. Rep. 2016-1. http://soccom.princeton.edu/sites/default/files/files/SOCCOM_2016-1_Bio-opticsprimer.pdf.

Bowie, A. R., D. Lannuzel, T. A. Remenyi, T. Wagener, P. J. Lam, P. W. Boyd, C. Guieu, A. T. Townsend, and T. W. Trull (2009), Biogeochemical iron budgets of the Southern Ocean

south of Australia: Decoupling of iron and nutrient cycles in the subantarctic zone by the summertime supply, Global Biogeochem Cy, 23.

Bowie, A. R., et al. (2015), Iron budgets for three distinct biogeochemical sites around the Kerguelen Archipelago (Southern Ocean) during the natural fertilisation study, KEOPS-2, Biogeosciences, 12(14), 4421-4445.

Boyd, P. W., and M. J. Ellwood (2010), The biogeochemical cycle of iron in the ocean, Nat Geosci, 3(10), 675-682.

Boyd, P. W., et al. (2007), Mesoscale iron enrichment experiments 1993-2005: Synthesis and future directions, Science, 315(5812), 612-617.

Carranza, M., and S. Gille (2015), Southern Ocean wind-driven entrainment enhances satellite chlorophyll-a through the summer, Journal of Geophysical Research, 120(1), 304-323.

Cassar, N., M. L. Bender, B. A. Barnett, S. Fan, W. J. Moxim, H. Levy, and B. Tilbrook (2007), The Southern Ocean biological response to aeolian iron deposition, Science, 317(5841), 1067-1070.

Cassar, N., P. J. DiFiore, B. A. Barnett, M. L. Bender, A. R. Bowie, B. Tilbrook, K. Petrou, K. J. Westwood, S. W. Wright, and D. Lefevre (2011), The influence of iron and light on net community production in the Subantarctic and Polar Frontal Zones, Biogeosciences, 8(2), 227-237.

Chang, C. H., N. C. Johnson, and N. Cassar (2014), Neural network-based estimates of Southern Ocean net community production from in situ O_2/Ar and satellite observation: a methodological study, Biogeosciences, 11(12), 3279-3297.

Dave, A. C., and M. S. Lozier (2013), Examining the global record of interannual variability in stratification and marine productivity in the low-latitude and mid-latitude ocean, Journal of Geophysical Research-Oceans, 118(6), 3114-3127.

de Boyer Montegut, C., G. Madec, A. S. Fischer, A. Lazar, and D. Iudicone (2004), Mixed layer depth over the global ocean: An examination of profile data and a profile-based climatology, Journal of Geophysical Research-Oceans, 109(C12).

Dong, S., J. Sprintall, S. T. Gille, and L. Talley (2008), Southern Ocean mixed-layer depth from Argo float profiles, Journal of Geophysical Research-Oceans, 113(C6).

Duce, R. A., and N. W. Tindale (1991), Atmospheric transport of iron and its deposition in the ocean, Limnology and Oceanography, 36(8), 1715-1726.

Dunne, J. P., R. A. Armstrong, A. Gnanadesikan, and J. L. Sarmiento (2005), Empirical and mechanistic models for the particle export ratio, Global Biogeochem Cy, 19(4).

Eveleth, R., N. Cassar, R. M. Sherrell, H. Ducklow, M. Meredith, H. Venables, Y. Lin, and Z. Li (2016), Ice melt influence on summertime net community production along the Western Antarctic Peninsula, Deep Sea Research Part II.

Fauchereau, N., A. Tagliabue, L. Bopp, and P. M. S. Monteiro (2011), The response of phytoplankton biomass to transient mixing events in the Southern Ocean, Geophys Res Lett, 38.

Fletcher, S. E. M., et al. (2006), Inverse estimates of anthropogenic CO_2 uptake, transport, and storage by the ocean, Global Biogeochem Cy, 20(2).

Frolicher, T. L., J. L. Sarmiento, D. J. Paynter, J. P. Dunne, J. P. Krasting, and M. Winton (2015), Dominance of the Southern Ocean in anthropogenic carbon and heat uptake in CMIP5 models, J Climate, 28(2), 862-886.

Frost, B. W. (1991), The role of grazing in nutrient-rich areas of the open sea, Limnology and Oceanography, 36(8), 1616-1630.

Graham, R. M., A. M. De Boer, E. van Sebille, K. E. Kohfeld, and C. Schlosser (2015), Inferring source regions and supply mechanisms of iron in the Southern Ocean from satellite chlorophyll data, Deep-Sea Res Pt I, 104, 9-25.

Hauck, J., and C. Volker (2015), Rising atmospheric CO_2 leads to large impact of biology on Southern Ocean CO_2 uptake via changes of the Revelle factor, Geophys Res Lett, 42(5), 1459-1464.

Johnson, R., P. G. Strutton, S. W. Wright, A. McMinn, and K. M. Meiners (2013), Three improved satellite chlorophyll algorithms for the Southern Ocean, Journal of Geophysical Research-Oceans, 118(7), 3694-3703.

Johnson, K. S., Plant, J. N., Coletti, L. J., Jannasch, H. W., Sakamoto, C. M., Riser, S. C., Swift, D. D., Williams, N. L., Boss, E., Haëntjens, N., Talley, L. D., and Sarmiento, J. L. (2017), Biogeochemical sensor performance in the SOCCOM profiling foat array. Journal of Geophysical Research: Oceans, 122 (8), 6416-6436.

Kahru, M., Z. Lee, and B. G. Mitchell (2017), Contemporaneous disequilibrium of bio-optical properties in the Southern Ocean, Geophys Res Lett, 2016GL072453.

Landschutzer, P., et al. (2015), The reinvigoration of the Southern Ocean carbon sink, Science, 349(6253), 1221-1224.

Lannuzel, D., V. Schoemann, J. de Jong, J. L. Tison, and L. Chou (2007), Distribution and biogeochemical behaviour of iron in the East Antarctic sea ice, Mar Chem, 106(1-2), 18-32.

Lannuzel, D., V. Schoemann, J. de Jong, L. Chou, B. Delille, S. Becquevort, and J. L. Tison (2008), Iron study during a time series in the western Weddell pack ice, Mar Chem, 108(1-2), 85-95.

Laws, E. A., P. G. Falkowski, W. O. Smith, H. Ducklow, and J. J. McCarthy (2000), Temperature effects on export production in the open ocean, Global Biogeochemical Cycles, 14(4), 1231-1246.

Li, Z., and N. Cassar (2016), Satellite estimates of net community production based on O_2/Ar observations and comparison to other estimates, Global Biogeochemical Cycles, 30(5), 735-752, https://doi.org/10.1002/2015GB005314.

Li, Z., N. Cassar, K. Huang, H. Ducklow, and O. Schofield (2016), Interannual variability in net community production at the Western Antarctic Peninsula region (1997-2014), Journal of Geophysical Research, 121(7), 4748-4762, https://doi.org/10.1002/2015JC011378.

Li, Z., and N. Cassar (2017), A mechanistic model of an upper bound on oceanic carbon export as a function of mixed layer depth and temperature, Biogeosciences, 14(22), 5015-5027, https://doi.org/10.5194/bg-14-5015-2017.

Li, Z., and N. Cassar (2018), Theoretical considerations on factors confounding the interpretation of the oceanic carbon export ratio, Global Biogeochemical Cycles, 32(11), 1644-1658, https://doi.org/10.1029/2018GB006003.

Llort, J., M. Lévy, J. B. Sallée, and A. Tagliabue (2019), Nonmonotonic response of primary production and export to changes in mixed-layer depth in the Southern Ocean, Geophysical Research Letters, 46(6), 3368-337, https://doi.org/10.1029/2018GL081788.

Lozier, M. S., A. C. Dave, J. B. Palter, L. M. Gerber, and R. T. Barber (2011), On the relationship between stratification and primary productivity in the North Atlantic, Geophys Res Lett, 38(18), https://doi.org/10.1029/2011GL049414.

Lunn, D. J., A. Thomas, N. Best, and D. Spiegelhalter (2000), WinBUGS - A Bayesian modelling framework: Concepts, structure, and extensibility, Stat Comput, 10(4), 325-337.

Majkut, J. D., J. L. Sarmiento, and K. B. Rodgers (2014), A growing oceanic carbon uptake: Results from an inversion study of surface pCO_2 data, Global Biogeochem Cy, 28(4), 335-351.

Martin, J. H., R. M. Gordon, and S. E. Fitzwater (1990), Iron in Antarctic waters, Nature, 345(6271), 156-158.

McGillicuddy, D. J., et al. (2015), Iron supply and demand in an Antarctic shelf ecosystem, Geophys Res Lett, 42(19), 8088-8097.

Mitchell, B. G., and O. Holm-Hansen (1991), Observations and modeling of the Antarctic phytoplankton crop in relation to mixing depth, Deep-Sea Res, 38(8-9), 981-1007.

Mitchell, B. G., E. A. Brody, O. Holm-Hansen, C. Mcclain, and J. Bishop (1991), Light limitation of phytoplankton biomass and macronutrient utilization in the Southern Ocean, Limnology and Oceanography, 36(8), 1662-1677.

Morel, A., H. Claustre, D. Antoine, and B. Gentili (2007), Natural variability of bio-optical properties in Case 1 waters: attenuation and reflectance within the visible and near-UV spectral domains, as observed in South Pacific and Mediterranean waters, Biogeosciences, 4(5), 913-925.

Munro, D. R., N. S. Lovenduski, T. Takahashi, B. B. Stephens, T. Newberger, and C. Sweeney (2015), Recent evidence for a strengthening CO_2 sink in the Southern Ocean from carbonate system measurements in the Drake Passage (2002-2015), Geophys Res Lett, 42(18), 7623-7630.

Nelson, D. M., and W. O. Smith (1991), Sverdrup revisited: Critical depths, maximum chlorophyll levels, and the control of Southern Ocean productivity by the irradiance-mixing regime, Limnology and Oceanography, 36(8), 1650-1661.

Orsi, A. H., T. Whitworth, and W. D. Nowlin (1995), On the Meridional Extent and Fronts of the Antarctic Circumpolar Current, *Deep-Sea Res Pt I*, *42*(5), 641-673.

Robinson, J., E. E. Popova, M. A. Srokosz, and A. Yool (2016), A tale of three islands: Downstream natural iron fertilization in the Southern Ocean, Journal of Geophysical Research.

Rohr, T., M. C. Long, M. T. Kavanaugh, K. Lindsay, and S. C. Doney (2017), Variability in the mechanisms controlling Southern Ocean phytoplankton bloom phenology in an ocean model

and satellite observations, Global Biogeochemical Cycles, 31(5), https://doi.org/10.1002/2016GB005615.

Sabine, C. L., et al. (2004), The oceanic sink for anthropogenic CO_2, Science, 305(5682), 367-371.

Schine, C. M. S., G. V. Dijken, and K. R. Arrigo (2016), Spatial analysis of trends in primary production and relationship with large-scale climate variability in the Ross Sea, Antarctica (1997–2013), Journal of Geophysical Research, 121(1), 368-386.

Sokolov, S., and S. R. Rintoul (2007), On the relationship between fronts of the Antarctic Circumpolar Current and surface chlorophyll concentrations in the Southern Ocean, Journal of Geophysical Research-Oceans, 112(C7).

Tagliabue, A., J. B. Sallee, A. R. Bowie, M. Levy, S. Swart, and P. W. Boyd (2014), Surface-water iron supplies in the Southern Ocean sustained by deep winter mixing, Nat Geosci, 7(4), 314-320.

Thomalla, S. J., N. Fauchereau, S. Swart, and P. M. S. Monteiro (2011), Regional scale characteristics of the seasonal cycle of chlorophyll in the Southern Ocean, Biogeosciences, 8(10), 2849-2866.

Uchida, T., D. Balwada, R. Abernathey, G. McKinley, S. Smith, and M. Lévy (2019), The contribution of submesoscale over mesoscale eddy iron transport in the open Southern Ocean, Journal of Advances in Modeling Earth Systems, 11(12), 3934-3958.

Uchida, T., D. Balwada, R. Abernathey, G. McKinley, S. Smith and M. Lévy (2020), Vertical iron fluxes support primary production in the open Southern Ocean, Nature Comm., 11, https://doi.org/10.1038/s41467-020-14955-0.

Volk, T., and M. I. Hoffert (1985), Ocean Carbon Pumps: Analysis of relative strengths and efficiencies in ocean-driven atmospheric CO_2 changes, in The Carbon Cycle and Atmospheric CO_2: Natural Variations Archean to Present, Geophys. Monogr. Ser., edited by E.T. Sundquist and W. S. Broecker, AGU, Washington, D. C., 1985., 32, 99-110.

Wilson, C., and V. J. Coles (2005), Global climatological relationships between satellite biological and physical observations and upper ocean properties, Journal of Geophysical Research-Oceans, 110(C10).

Figure 1. Climatological NCP in the Southern Ocean between 1997 and 2020. Solid black, gray, black-dashed, and gray-dashed lines represent the climatological position of the Subtropical Front, Subantarctic Front, Polar Front, and Southern Antarctic Circumpolar Current Front, respectively (according to *Orsi et al.* [1995]). White areas in high latitudes are covered by sea ice. NCP is shown on a logarithmic scale.

Figure 2. Heteroscedastic relation of particulate organic carbon (POC) concentration vs. mixed layer depth (MLD) in austral Spring, Summer, Autumn, and Winter, and all seasons. Points are color coded for the density of observations.

Figure 3. Changes in POC (ΔPOC) as a function of shoaling mixed layer (ΔMLD) above the critical depth in austral (A) spring, (B) summer, (C) autumn, and (D) winter. N and ΔPOC>0 represent the number of points and the percentage of points showing increases in POC, respectively. Points above the dashed lines (ΔPOC=0) show increases in POC. POC is log-transformed before calculating the difference. Points are color coded for the density of observations. Changes in POC and MLD (10 day changes) are calculated using biogeochemical Argo floats which can be accessed online at https://soccom.princeton.edu/.

Figure 4. Spearman correlation coefficients between monthly climatological NCP, (A) mixed layer depth, and (B) mixed-layer-averaged PAR. Solid black, gray, black-dashed, and gray-dashed lines represent the Southern Ocean fronts, as described in Figure 1. White areas represent correlations with $p>0.1$ and missing data.

Figure 5. Spearman correlation coefficients between monthly anomalies of NCP, (A-D) mixed layer depth, and (E-H) mixed-layer-averaged PAR in austral (A and E) spring, (B and F) summer, (C and G) autumn, and (D and H) winter. Solid black, gray, black-dashed, and gray-dashed lines represent the Southern Ocean fronts, as described in Figure 1. White areas represent correlations with p>0.1 and missing data.

Figure 6. Spearman correlation coefficients between winter mixed layer depth anomalies derived from Argo floats and average NCP anomalies in austral (A) spring and (B) summer. Solid black, gray, black-dashed, and gray-dashed lines represent the Southern Ocean fronts, as described in Figure 1. White areas represent correlations with p>0.1 and missing data.

Figure 7. Long-term trends in annual NCP for the entire Southern Ocean (A) and by region (B). (C) Percentage of long-term trend compared to annual NCP interannual variability (as a measure of the signal to noise ratio). Grey shaded area in (A) represents the time period associated with the study of *Landschutzer et al*. [2015]. White areas in subplots (B-C) represent missing data (mainly in high-latitude regions) or not statistically significance with $p > 0.1$. Solid black, gray, black-dashed, and gray-dashed lines represent the Southern Ocean fronts, as described in Figure 1.

Figure1.

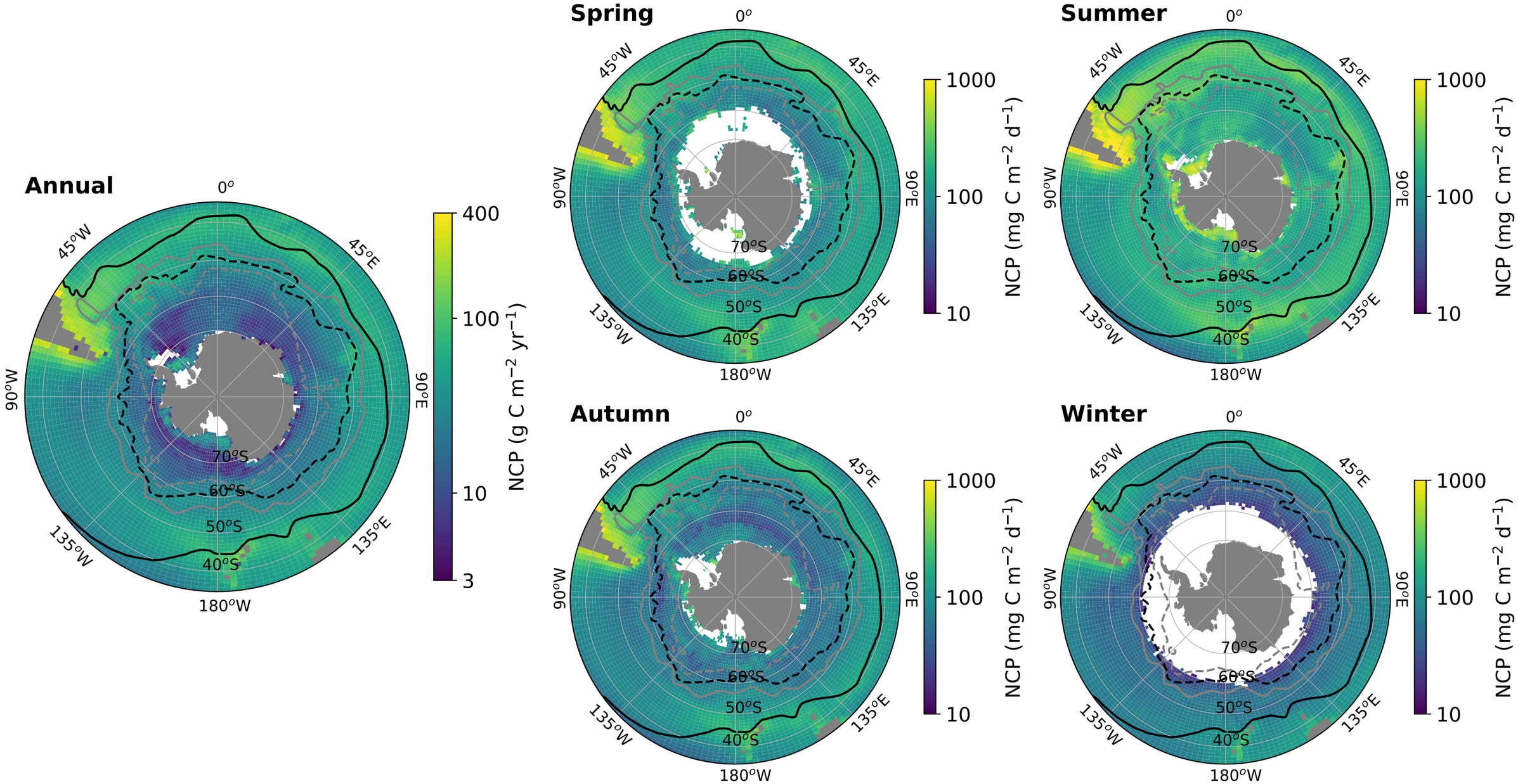
Annual
Spring
Summer
Autumn
Winter
0°
45°W
45°E
90°W
90°E
135°W
135°E
180°W
70°S
60°S
50°S
40°S
400
100
10
3
1000
NCP (g C m^{-2} yr^{-1})
NCP (mg C m^{-2} d^{-1})

Figure2.

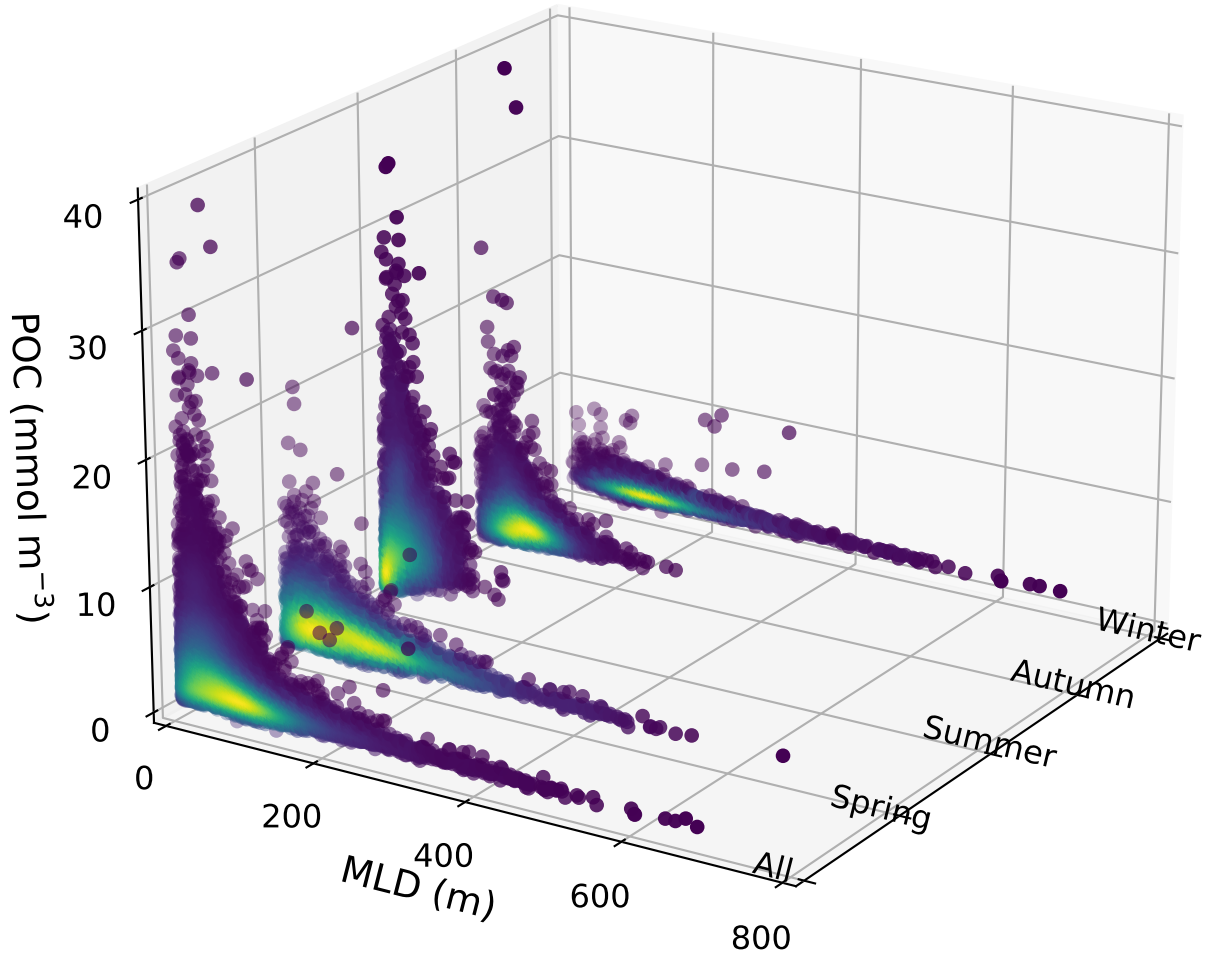
POC (mmol m^{-3})
0
10
20
30
40
MLD (m)
0
200
400
600
800
Winter
Autumn
Summer
Spring
All

Figure3.

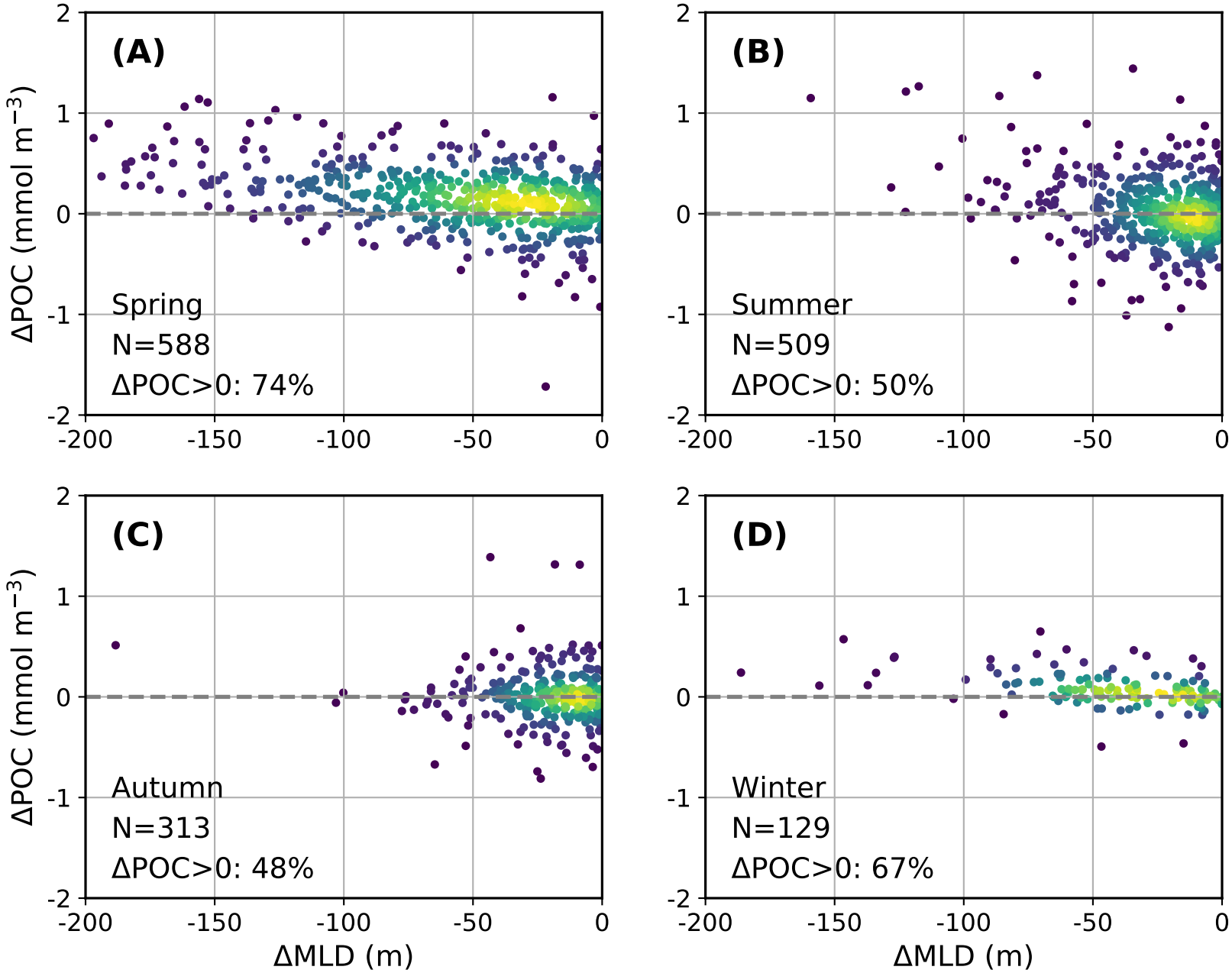
(A)
Spring
N=588
ΔPOC>0: 74%
(B)
Summer
N=509
ΔPOC>0: 50%
(C)
Autumn
N=313
ΔPOC>0: 48%
(D)
Winter
N=129
ΔPOC>0: 67%
ΔPOC (mmol m^{-3})
ΔMLD (m)
2
1
0
-1
-2
-200
-150
-100
-50
0

Figure 4.

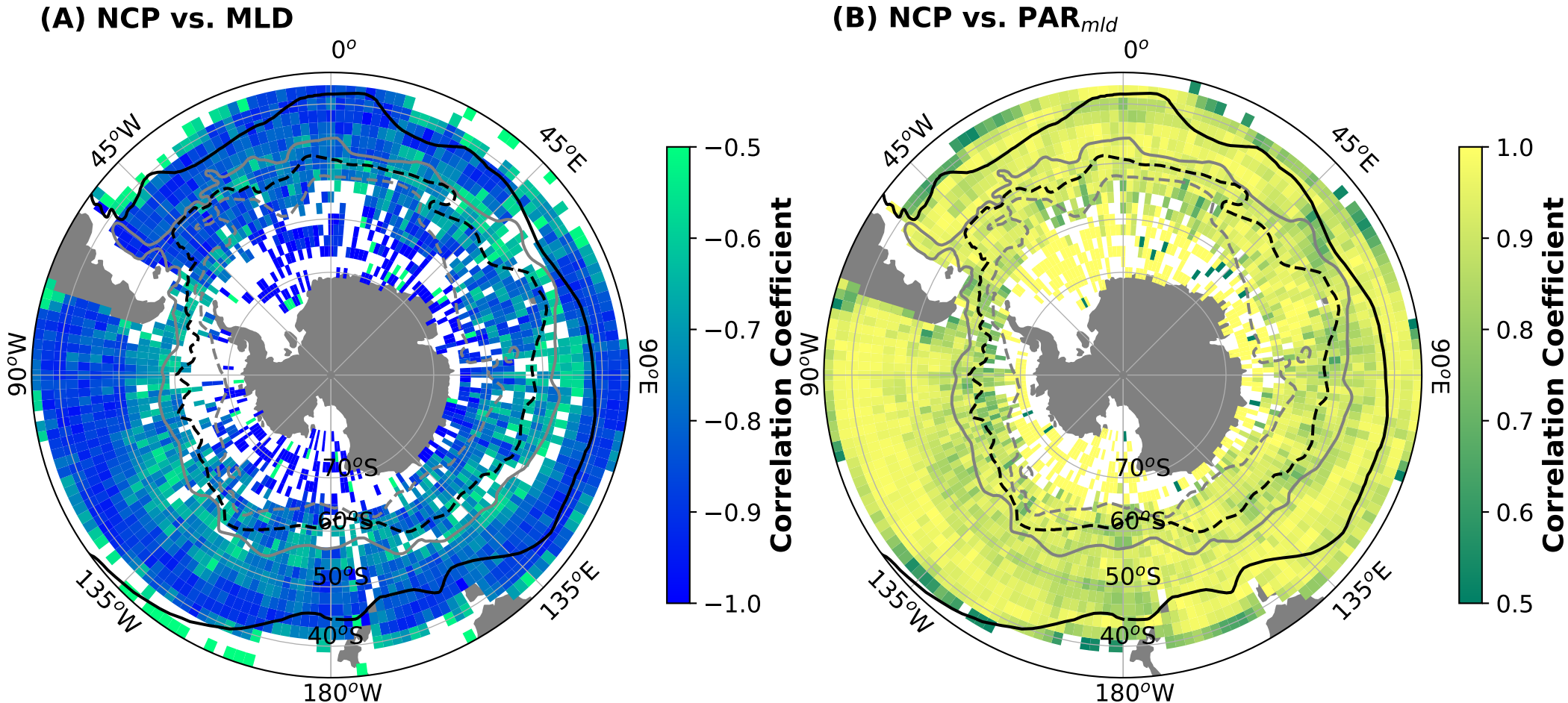
(A) NCP vs. MLD
0°
45°W
45°E
90°W
90°E
135°W
135°E
180°W
70°S
60°S
50°S
40°S
−0.5
−0.6
−0.7
−0.8
−0.9
−1.0
Correlation Coefficient
(B) NCP vs. PAR$_{mld}$
0°
45°W
45°E
90°W
90°E
135°W
135°E
180°W
70°S
60°S
50°S
40°S
1.0
0.9
0.8
0.7
0.6
0.5
Correlation Coefficient

Figure 5.

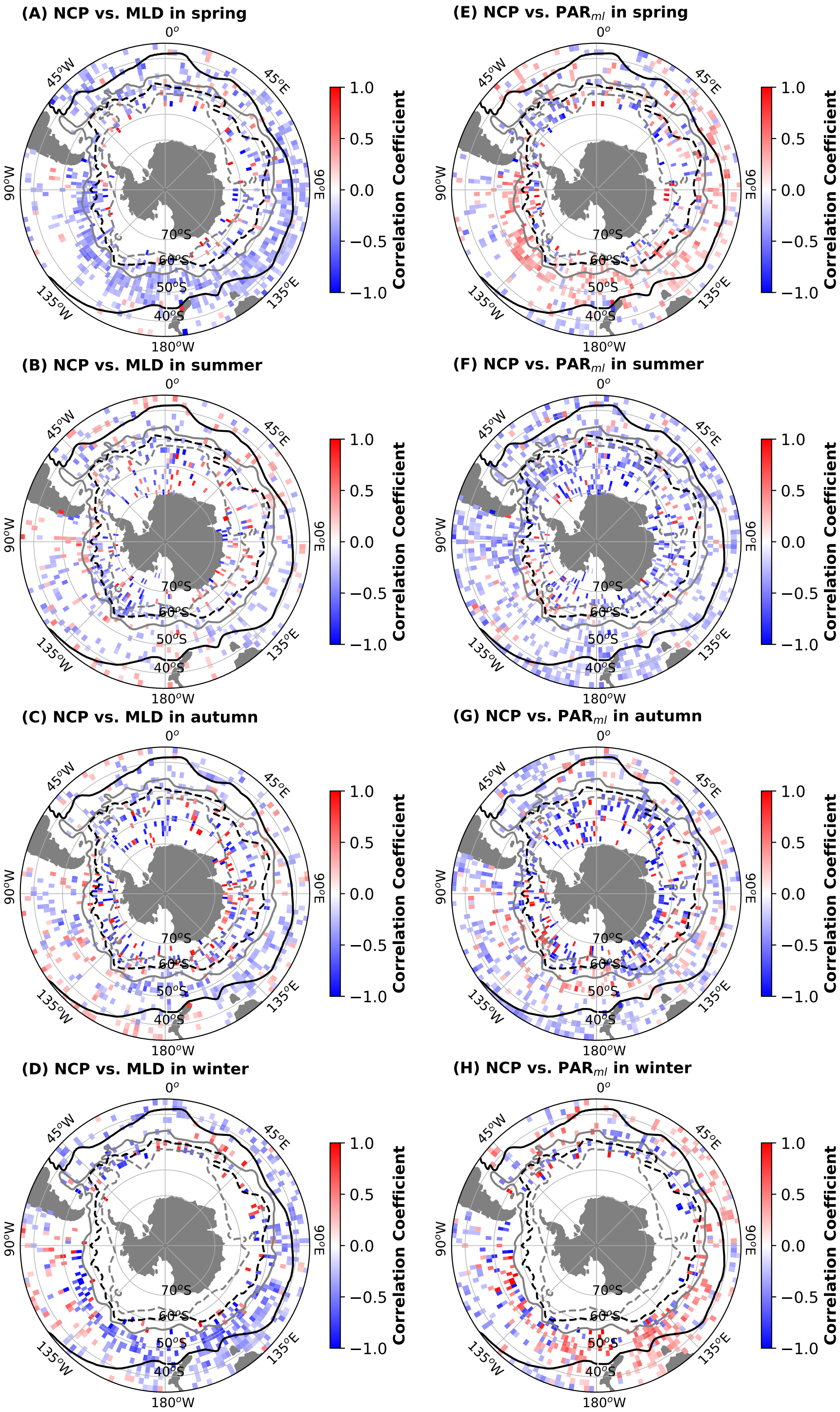
(A) NCP vs. MLD in spring
(E) NCP vs. PAR$_{ml}$ in spring
(B) NCP vs. MLD in summer
(F) NCP vs. PAR$_{ml}$ in summer
(C) NCP vs. MLD in autumn
(G) NCP vs. PAR$_{ml}$ in autumn
(D) NCP vs. MLD in winter
(H) NCP vs. PAR$_{ml}$ in winter
0°
45°W
45°E
90°W
90°E
135°W
135°E
180°W
70°S
60°S
50°S
40°S
1.0
0.5
0.0
−0.5
−1.0
Correlation Coefficient

Figure 6.

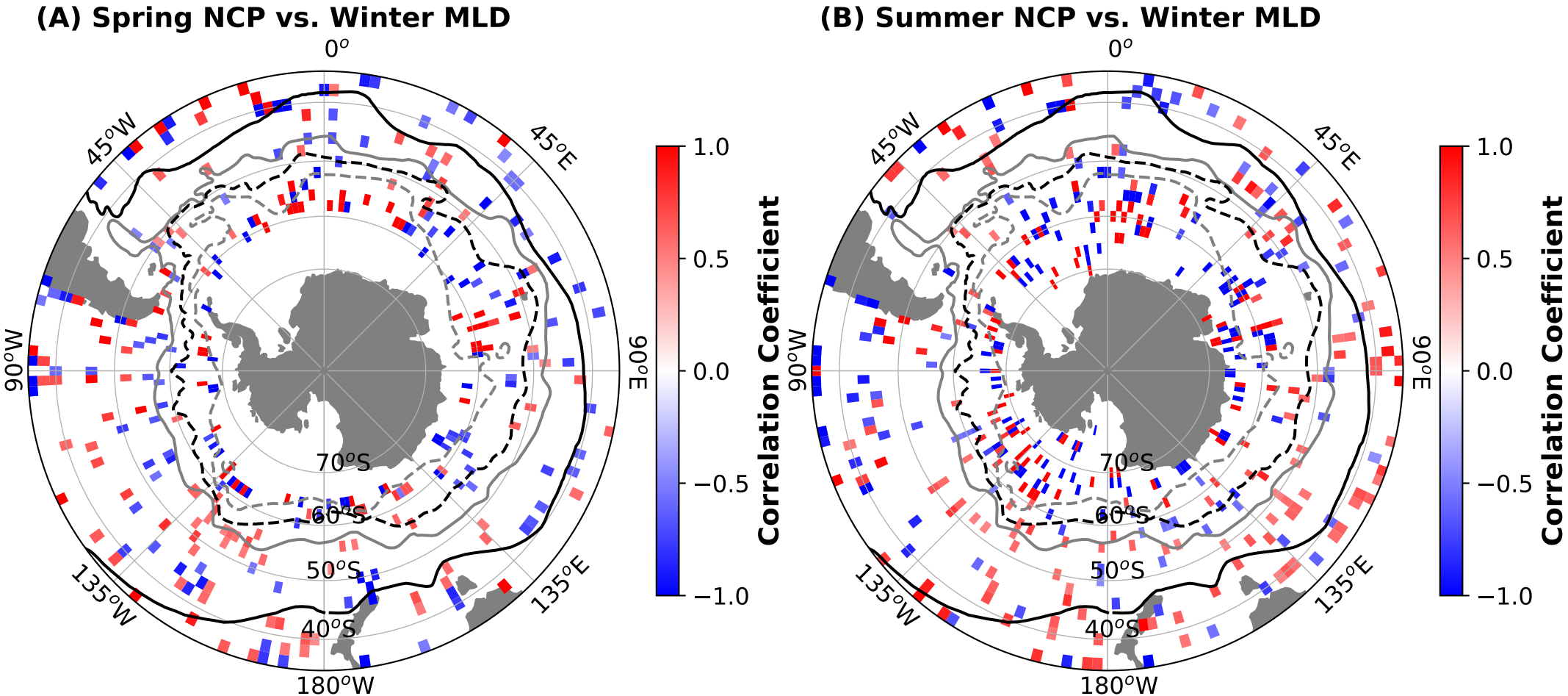
(A) Spring NCP vs. Winter MLD
(B) Summer NCP vs. Winter MLD
0°
45°W
45°E
90°W
90°E
135°W
135°E
180°W
70°S
60°S
50°S
40°S
1.0
0.5
0.0
−0.5
−1.0
Correlation Coefficient

Figure 7.

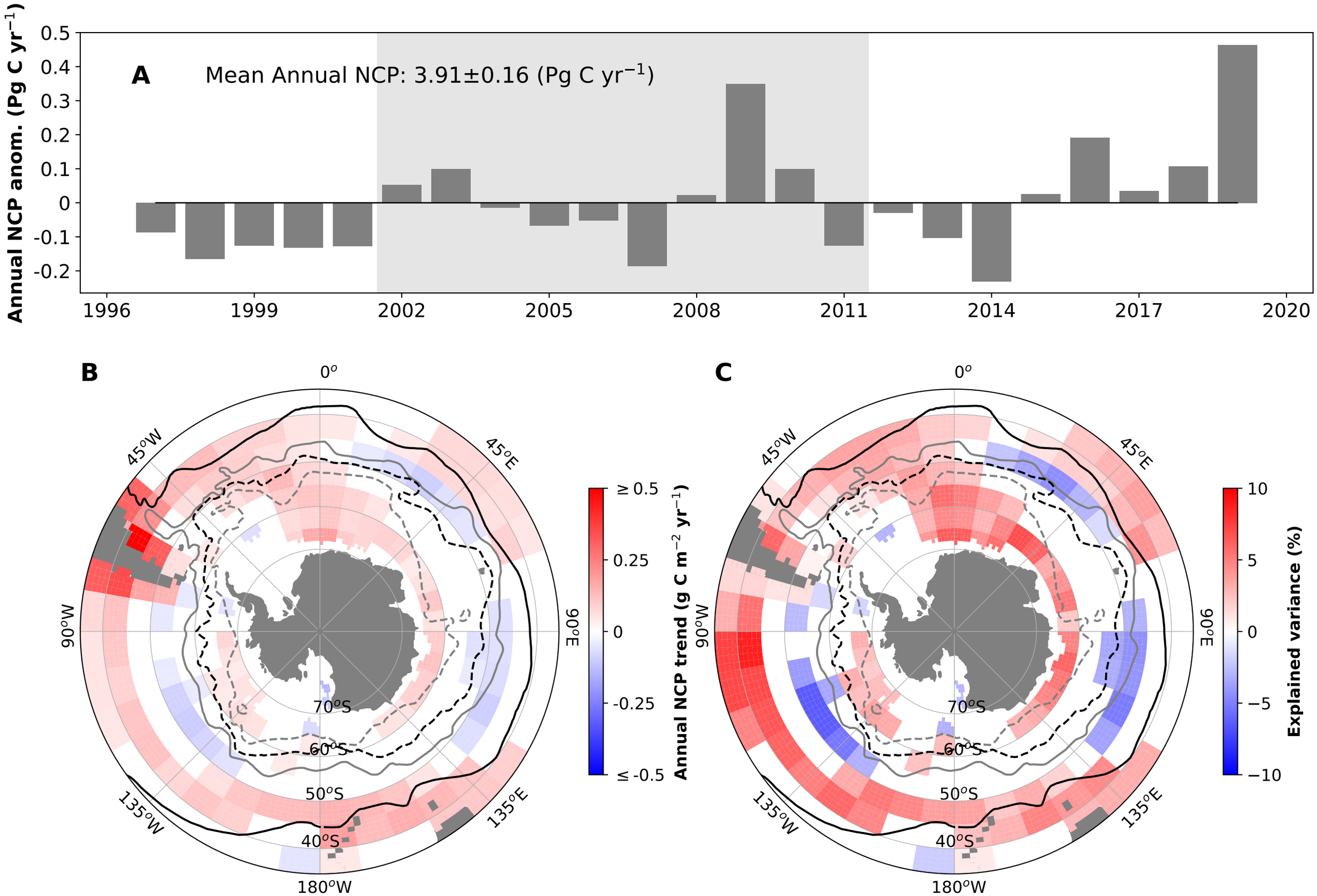
A
Mean Annual NCP: 3.91±0.16 (Pg C yr^{-1})
Annual NCP anom. (Pg C yr^{-1})
0.5
0.4
0.3
0.2
0.1
0
-0.1
-0.2
1996
1999
2002
2005
2008
2011
2014
2017
2020
B
C
0°
45°E
90°E
135°E
180°W
135°W
90°W
45°W
70°S
60°S
50°S
40°S
≥ 0.5
0.25
0
-0.25
≤ -0.5
Annual NCP trend (g C m^{-2} yr^{-1})
10
5
0
−5
−10
Explained variance (%)